Materials Today Catalysis 9 (2025) 100093

Contents lists available at ScienceDirect

Materials Today Catalysis

journal homepage: www.journals.elsevier.com/materials-today-catalysis

Improved low-temperature CO oxidation using heterogeneous nanofibrous structures decorated with Pd atoms and nanocrystals

M.A. Rodriguez-Olguin [a,*], D. Cazac [a], F. Ruiz-Zepeda [b,c], S. Bartling [d], M. Bosco [e,f], H. Atia [d], R. Eckelt [d], A. Manzo-Robledo [g], M. Vandichel [h], A. Aguirre [a,f,**], J.G.E. Gardeniers [a,*], A. Susarrey-Arce [a,*]

[a] *Department of Chemical Engineering, Mesoscale Chemical Systems, MESA+Institute, University of Twente, P.O. Box 217, Enschede 7500AE, the Netherlands*
[b] *Department of Materials Chemistry, National Institute of Chemistry, Hajdrihova 19, Ljubljana 1000, Slovenia*
[c] *Department of Physics and Chemistry of Materials, Institute of Metals and Technology, Lepi pot 11, Ljubljana, Slovenia*
[d] *Leibniz Institute for Catalysis, Albert-Einstein-Straße 29a, Rostock D-18059, Germany*
[e] *Instituto de Desarrollo Tecnológico para la Industria Química, Universidad Nacional del Litoral, CONICET, Güemes 3450, Santa Fe S3000GLN, Argentina*
[f] *Facultad de Ingeniería Química, Universidad Nacional del Litoral, Santiago del Estero 2829, Santa Fe 3000, Argentina*
[g] *Instituto Politécnico Nacional, Laboratorio de Electroquímica y Corrosión, Escuela Superior de Ingeniería Química e Industrias Extractivas, Av. Instituto Politécnico Nacional S/N, Unidad Profesional Adolfo López Mateos, CDMX, CP 07708, Mexico*
[h] *School of Chemical Sciences and Chemical Engineering, Bernal Institute, University of Limerick, Limerick V94 T9PX, Ireland*

ARTICLE INFO

Keywords:
Electrospinning
Pd nanocrystals
Alumina
Nanofibers
CO oxidation

ABSTRACT

Amorphous alumina shaped as nanofibers forming a non-woven network, functioning as a heterogeneous dispersion for palladium (Pd) atoms and nanocrystals, is unique yet unstudied for low-temperature CO oxidation. This work demonstrates that nanometric-size alumina fibers (ANFs) with a surface area of ~230 m^2/g can host Pd species that remain nearly intact after CO oxidation. The ANFs contain various Pd (Pd-ANFs) loadings, ranging from 1 %wt. (Pd1-ANFs), 3 %wt. (Pd3-ANFs), to 5 %wt. (Pd5-ANFs). Among them, Pd3-ANFs show the highest CO chemisorption. Hence, the chemical environment of the Pd3-ANFs is assessed using NAP-XPS under various CO and O_2 mixtures. NAP-XPS shows the presence of metallic and oxidized Pd species. The results are correlated with DRIFT spectroscopy, which unveils the CO species adsorbed over Pd. Furthermore, a computational-based kinetic model for CO oxidation shows that Pd single atoms start the CO-oxidation, followed by larger Pd crystals during light-off. Our results demonstrate that the Pd-ANFs have higher activity when compared with the Pd alumina nanoparticles (Pd-ANP) counterpart that lacks a fibrous structure, highlighting the benefits of the ANF's structural network in stabilizing atomic and nanometric scale metal catalysts for low-temperature CO oxidation.

1. Introduction

Al_2O_3 is a ceramic material with various crystalline forms [1–5] widely used in the industry [6,7]. Al_2O_3 supports provide acidity, surface area, and thermal stability, which are key characteristics in heterogeneous catalysis [8–11]. Synthetic approaches of Al_2O_3 focus on tuning microporosity (<2 nm pore width), mesoporosity (from 2 to 50 nm pore width), and macroporosity (>50 nm pore width) to the finest level to improve chemical conversion [6,12]. Catalysis synthesis advancements have not stopped at tuning micro-, meso-, and macro-pores. Structural shaping of Al_2O_3 forming microscale or millimetric size architectures while maintaining such multi-porosity characteristics has occurred over the years. The gap between such scales has been bridged using additive manufacturing (AM) methods, as in the case of Al_2O_3 monoliths [13–17]. The later methods enable the production of freeform geometrical architectures designed to control reaction rates via mass transfer and diffusivity. However, in some cases, the Al_2O_3 initial characteristics can be modified during manufacturing, perhaps due to

---

* Corresponding authors.
** Corresponding author at: Department of Chemical Engineering, Mesoscale Chemical Systems, MESA+ Institute, University of Twente, P.O. Box 217, Enschede 7500AE, the Netherlands.
E-mail addresses: m.rdzolg@gmail.com (M.A. Rodriguez-Olguin), aaguirre@santafe-conicet.gov.ar (A. Aguirre), j.g.e.gardeniers@utwente.nl (J.G.E. Gardeniers), a.susarreyarce@utwente.nl (A. Susarrey-Arce).

https://doi.org/10.1016/j.mtcata.2025.100093
Received 20 November 2024; Received in revised form 24 February 2025; Accepted 26 February 2025

the incompatibility between materials (e.g., stabilizers, binders, and surfactants). It is, therefore, essential to find ways to design Al_2O_3 geometrical forms without compromising the chemical properties of the Al_2O_3, e.g., acid sites [9,10], where reactants adsorb, guiding the transformation of molecules, which ultimately react and desorb from the catalyst's active site [8,10].

Reactions relying on mesoscopic geometries [13–15] can then be adapted to facilitate transport throughout multiple length scales to outpace intermediate instabilities leading to side products. This step can be reached by producing geometrical architectures. Aside from AM [17–20], electrospinning [10,21] offers the opportunity to produce fiber-like geometries of a few nanometers in diameter. Arranged in a non-woven fashion, nanofibers composed of Al_2O_3 [13–15] should ideally allow better inter- and intra-particle diffusion, overcoming possible mass transfer limitations and simultaneously permitting the deposition of highly dispersed Pd nanocrystals.

Different systems with nanoparticles (NPs) on different nanofiber substrates have been studied[22–25]. Only a few groups have demonstrated the ability to decorate amorphous Al_2O_3 nanofibers (hereafter ANFs) with Pd nanocrystals (Table S1). However, understanding Pd atoms and nanocrystal relationships for the CO oxidation reaction has not been explored in detail. An additional novelty is that the proposed ANF approach differs from conventional preparation methods, such as impregnation and coprecipitation, which typically utilize bulk Al_2O_3 of virtually any shape [26–29]. Furthermore, this research effort connects reaction steps occurring over metal catalysts (Pd atoms and nanocrystals) supported over shaped Al_2O_3 fiber geometry. Understanding the relationship between nanometric (i.e., Pd a few atoms and nanocrystals) and micrometric (i.e., non-woven nanofiber support) length scales during a chemical reaction is the knowledge that can be used as a staircase to connect with reaction steps [30].

This work presents a one-pot synthesis method using electrospinning to produce non-woven Pd-ANF architectures. The functionality of the non-woven nanofiber architecture is demonstrated by contrasting the Pd-ANFs with Pd-ANPs. Morphological analysis indicates higher Pd distribution in ANFs. The Pd has different oxidation states, as determined by NAP-XPS. The results are then compared with DRIFT spectroscopy, showing that adsorbed CO adopts several configurations, which vary between ANFs and ANPs. The functionality of Pd-ANFs and Pd-ANPs is assessed during CO oxidation under different CO and O_2 ratios. Light-off curves for CO oxidation demonstrate that the Pd-ANFs have higher activity when compared to their Pd-ANP counterparts, highlighting the importance of Pd-decorated structured support for low-temperature catalysis. Aided by *ab initio* kinetic modeling, we evidenced that Pd single-atoms help to start the low-temperature reaction followed by nanoparticle crystal contributions during light-off. The results are supported by STEM ADF analysis, in which single atoms are observed, even after the CO oxidation reaction.

2. Methodology

2.1. Synthesis of Pd nanoparticles on Al_2O_3 nanofibers with electrospinning

The Pd-ANFs were prepared using a commercial electrospinning system (IME Technologies, The Netherlands). The IME system was operated utilizing a stainless-steel needle (inner diameter of 0.4 mm) at a separation distance of 12 cm from the aluminum collector plate. First, a mixture consisting of 4 %w/v $C_{14}H_{27}AlO_5$ (ASB) technical grade from Alpha Aesar, 6 %w/v polyvinylpyrrolidone (PVP, MW ~1300,000), and 0.53 %w/v t-octylphenoxypolyethoxyethanol (Triton x100, Sigma-Aldrich) dissolved in ethanol (100 % Tech. grade, BOOM BV, The Netherlands) was used as the aluminum precursor solution to generate ANFs. Pd acetate (ACS, Sigma-Aldrich) was used as Pd source. Three different Pd acetate concentrations were used (0.0002, 0.0005, 0.0014 %w/v) and incorporated into the ASB precursor solution during mixing (1 h). The concentrations of Pd acetate used are equivalent to 1, 3, and 5 % w/w of Pd in Al_2O_3. The prepared solutions were electrospun at environmental temperature and controlled humidity (35 %) using a potential of 19 kV and at 5 mL/h infusion rate. After deposition, all fiber samples were dried in an oven for 12 h at 353 K to remove the excess solvent. Subsequently, they were calcined (Nabertherm LH 15/12) in air with a temperature ramp of 1 K/min to 623 K for 3 h and then 1 K/min until reaching 773 K for 1 h. The synthesized nanofiber catalysts were labeled, Pd1-ANF, Pd3-ANF, and Pd5-ANF. ANP control catalysts containing 1, 3, and 5 % w/w of Pd were also prepared by drop-casting using the same ASB and Pd acetate precursor solutions. These ANP samples were annealed following the same procedure as the ANFs and labeled as Pd1-ANP, Pd3-ANP, and Pd5-ANP for simplicity.

2.2. Morphological characterization

The morphology of the ANF and ANP were analyzed using a high-resolution (HR) SEM microscope (Zeiss MERLIN) operated at 1.40 kV coupled with a High-Efficiency Secondary Electron Detector (HE-SE2). Before SEM analysis, samples were sonicated in ethanol, leading to nanofiber fragmentation into smaller pieces.

Annular dark field (ADF) scanning transmission electron microscopy (STEM) images were collected in bright field (BF) using an aberration-corrected JEOL ARM 200CF Transmission Electron Microscope operated at 80 kV. Energy Dispersive X-ray Spectroscopy maps were collected using a JEOL Centurio 100 mm^2 detector. Samples for (S)TEM were prepared by dispersing 5 mg of either Pd-ANFs or Pd-ANPs in ethanol and sonicated for 5 min. The suspension was dropcasted on Cu grids.

2.3. Structural characterization

The crystalline structure was analyzed by X-ray powder diffraction (D2 PHASER, Bruker) using Cu Kα radiation ($\lambda = 1.5418$ Å) operated at 30 kV, 10 mA, in the 2θ range between 10 and 70°, employing at 0.05° step-size and a scan speed of 0.1°/s. A Si-low background sample holder (Bruker) was used for the hybrid samples.

2.4. Surface area and porosity

The BET surface area and pore diameter of the Pd-ANFs or Pd-ANPs were determined from the nitrogen adsorption/desorption isotherms at 77 K on a Micrometrics ASAP 2010 instrument. Before the measurement, each sample was evacuated at 473 K for 4 h. The pore size distributions was calculated using the Barrett-Joyner-Halenda (BJH) method [31].

2.5. CO chemisorption analysis

The measurement was done using a 3-Flex Micromeritics instrument for the CO-Pulse chemisorption experiments. A 150 mg sample was loaded into a U-shaped quartz reactor and heated from RT to the corresponding reduction temperature (573 K) with 5 K/min in 5 % H_2/Ar (50 mL/min) for 120 min. Afterward, gas was changed to He (50 mL/min), and the sample was flushed for 90 min and then cooled to RT. After that, the sample loop was filled with 20 % CO/He, and then pulses were initiated onto the sample using He as carrier gas (50 mL/min). The peaks were recorded and integrated using a TCD detector, assuming a chemisorption stoichiometry metal surface: CO = 2 and a spherical shape of the metal particle.

2.6. FTIR measurements of CO adsorption and CO oxidation

FTIR in DRIFT-*operando* mode was used to investigate the adsorption (FTIR-CO) and oxidation of CO over the Pd-ANFs and Pd-ANPs. In both cases, 20 mg of the catalyst was loaded into the DRIFT cell (Harrick, modified). The cell was mounted into the Praying Mantis diffuse reflection accessory (Harrick) inside the sample compartment of the FTIR spectrometer (Thermo-Electron, Nicolet 8700 with a cryogenic MCT detector). The bench of the spectrometer was continuously purged with dried air (Parker Balston FTIR purge gas generator) to eliminate CO_2 and water vapor contributions to the spectra. Time-resolved DRIFT spectra were recorded at a resolution of 4 cm^{-1} (up to 1 spectrum/ 0.39 s). The exit of the cell was connected to a mass spectrometer Prisma QMG220 (Pfeiffer) by a sampling capillary. A flow-through 10-way valve, electronically actuated (Vici-Valco) and synchronized with the FTIR, controlled the entrance of the gases . The flow rate was regulated by mass flow meters (Cole-Parmer)[32].

The followed experimental protocol is described in Scheme 1. The samples were activated by flowing H_2 (5 % in He) at 573 K (2 h, 5 K/ min) and cooling down in He (**Step A**). CO adsorption (**Step B**), CO was adsorbed by flowing CO (1 % in He) 50 mL/min at 323 K over the reduced samples. After the CO adsorption in **Step B**, the oxidation of the pre-adsorbed CO was carried out by flowing O_2 (5 % in He). CO oxidation (**Step C**) was studied using different α_{CO} values to study the effect of the CO/O_2 ratio, where $\alpha_{CO} = \frac{p_{CO}}{p_{CO}+p_{O_2}}$. Three different α_{CO} (0.1, 0.2, 0.5) conditions were tested in series. The total flow was 50 mL/min, and the temperature was changed from 350 to 453 K. After the testing of each α_{CO}, the reactor was allowed to cool down until 323 K. For reference; CO adsorption was also carried out on non-reduced (PdO) samples.

2.7. *Near ambient pressure (NAP) – XPS*

Operando X-ray photoelectron spectroscopy (XPS) measurements were performed with a near-ambient pressure X-ray photoelectron spectroscopy system (NAP-XPS, SPECS Surface Nano Analysis GmbH, Germany). The setup has a differentially pumped Phoibos 150 electron energy analyzer with a nozzle of 500 μm, a monochromated Al Kα radiation source (E = 1486.6 eV), and a laser heating system for sample heating. The analysis chamber can be filled by five mass flow controllers (Brooks, GF40) with different gases and reaction mixtures up to a total pressure of 10 mbar; for the current experiments, a total pressure of 2 mbar is used. Reaction gases and formed products were monitored using a mass spectrometer (QMS, MKS e-vision 2) attached to the lens system of the spectrometer (lens 1). The powder samples are pressed into flakes using a laboratory press with 10 mm diameter and a load of about 0.5 t and mounted on the sample plate using a metal mesh and a circular aperture to minimize charging. Temperature is monitored by a thermocouple on the sample plate pressed to the sample surface.

A description of the experimental protocol is shown in Scheme 2. The samples were activated by flowing H_2 (10 % in He) at 600 K (2 h, 5 K/ min) and cooling down to 350 K in He (**Step A**). CO adsorption (**Step B**): CO was adsorbed by flowing CO (1 % in He) at 350 K for 1.5 h over the reduced samples. Later, the CO concentration was increased (5 % in He) to adjust the CO concentration to $\alpha_{CO} = 0.2$. CO oxidation (**Step C**): CO oxidation was carried out using different temperatures (350, 450, 550, and 600 K) at $\alpha_{CO} = 0.2$. Each oxidation temperature was studied for about 1 h.

Ex-situ XPS was carried out using an ESCALAB 220iXL (Thermo Fisher Scientific) with monochromated Al Kα radiation (E = 1486.6 eV). ANFs and ANPs loaded with Pd were prepared on a stainless-steel holder with conductive double-sided adhesive carbon tape. The electron binding energies were obtained with charge compensation using a flood electron source. In both cases (*in-situ* and ex-situ), data are referenced to the C 1 s core level of carbon at 284.8 eV (C-C and C-H bonds). The peaks were deconvoluted with Gaussian-Lorentzian curves using the Unifit 2021 software for quantitative analysis. The peak areas were normalized by the spectrometer's transmission function and Scofield's element-specific sensitivity factor.

3. Results and discussions

3.1. *Supported Pd nanocrystals on Al_2O_3 nanofibers*

Previous reports demonstrate that the nanofibers are produced using ASB as an alumina precursor[9,10]. A slight modification from our methodology is that Pd acetate is added to the electrospinning ASB precursor solution[9,10]. The rationale behind such a step is to load the ANF with Pd nanocrystals at the start without needing an additional catalyst loading step. We then proceed with preparing three independent precursor solutions with final Pd loadings of 1 %wt. (Pd1-ANF), 3 %wt. (Pd3-ANF), and 5 % wt. (Pd5-ANF). Once the precursor is electrospun, the nanofibers are annealed under an air atmosphere at 773 K for 1 h.

The SEM images of the annealed nanofibers (Pd1-ANF, Pd3-ANF, and Pd5-ANF) show a non-woven fiber morphology (Fig. 1**a**-1**c**) with ANFs diameters of 170 ± 41 nm for Pd1-ANF, 203 ± 61 nm for Pd3-ANF, and 241 ± 37 nm for Pd5-ANF. Three additional Pd-loaded Al_2O_3 samples are synthesized to benchmark the importance of ANF geometry. Instead of electrospinning, the precursor solution is drop-casted into crucibles and annealed in an air atmosphere. Three catalysts are obtained with final Pd loadings of 1 %wt. (Pd1-ANP), 3 %wt. (Pd3-ANP), and 5 % wt. (Pd5-ANP). SEM images for Pd-ANP reveal a particle-like morphology (Figs. 1**d**-1**f**).

From the SEM images in Fig. 1, evaluating the presence of Pd nanocrystals in ANFs and ANPs is challenging. However, the catalysts in Fig. 1 comprise amorphous Al_2O_3 and PdO, as identified with XRD; the results are shown in Figure S1. Furthermore, the ANFs and ANP with PdO treated under H_2/He are inspected with STEM to identify the nanocrystal sizes (Fig. 2). Figs. 2**a,** 2**c,** and 2**e** show Pd1-ANF, Pd3-ANF, and Pd5-ANF pre-treated in 5 % H_2/He following **step A** in Scheme 1. Figs. 2**b,** 2**d,** and 2**f** show Pd1-ANF, Pd3-ANF, and Pd5-ANF after the CO oxidation (**step C**, Scheme 1). The Pd particle size distribution for **step A** is presented in Fig. 2**a', 2c'**, and **2e'**. The nanocrystal size distribution for **step C** is presented in Fig. 2**b', 2d'**, and **2 f'**. It should be noted that the reduction treatment in H_2 has no apparent influence on the nanocrystal shape when compared, for example, to the Pd3-ANF treated

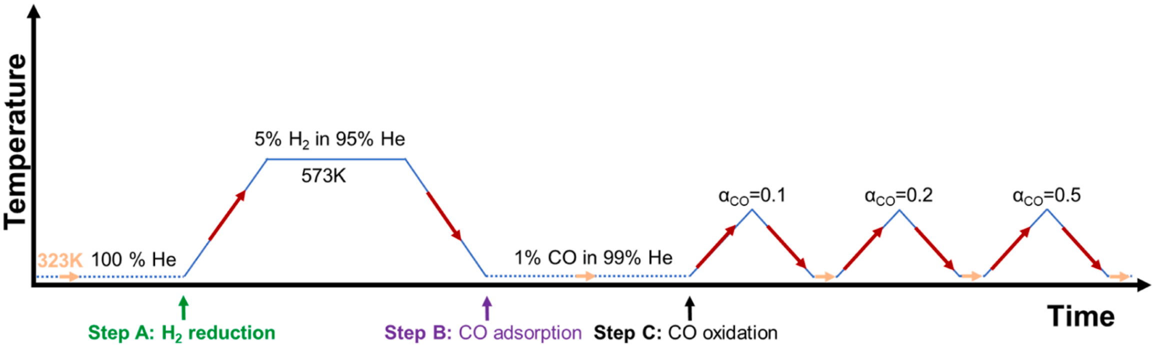

Scheme 1. Experimental scheme of the CO-FTIR adsorption and CO oxidation at 323 K using various α_{CO} ratios (α_{CO} = 0.1, 0.2, 0.5) experiments.

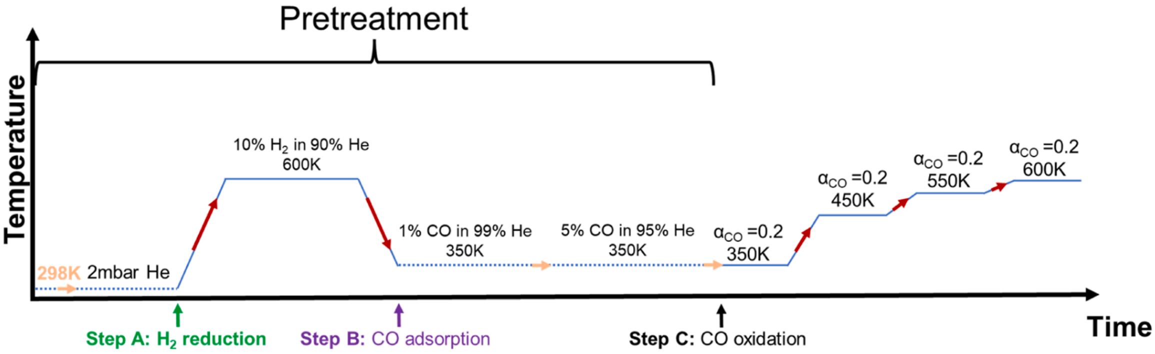

Scheme 2. Experimental scheme of the NAP-XPS experiments during CO oxidation using $\alpha_{CO} = 0.2$ at different temperatures.

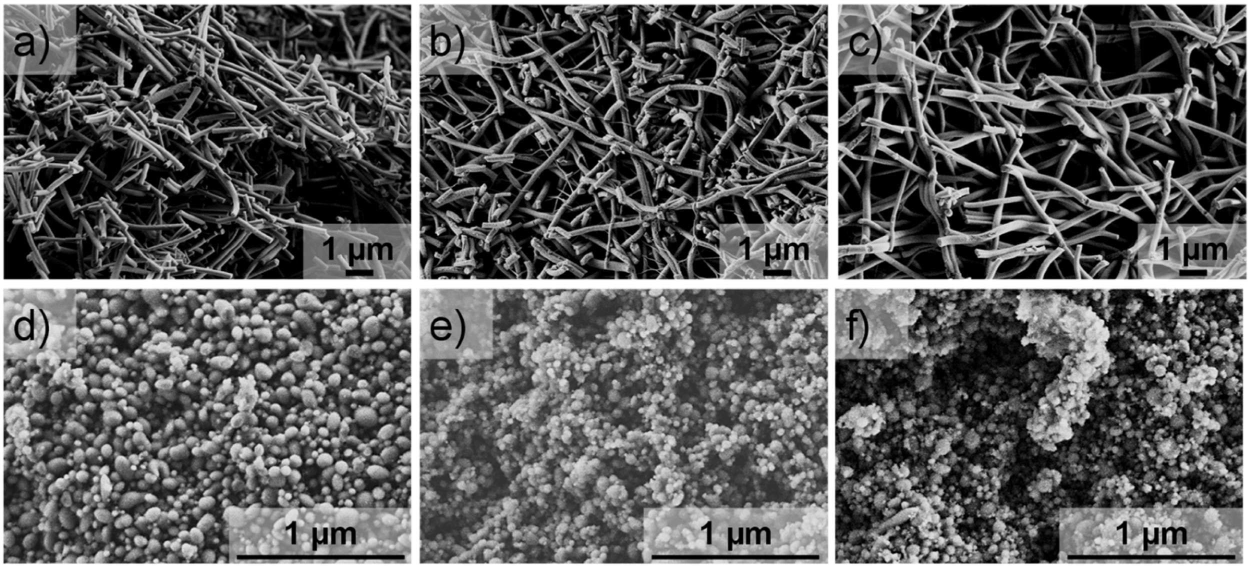

Fig. 1. SEM images of (**a**) Pd1-ANF, (**b**) Pd3-ANF, (**c**) Pd5-ANF, (**d**) Pd1-ANP, (**e**) Pd3-ANP, and (**f**) Pd5-ANP after annealing in air. It should be noted that SEM images in (**a-c**) are broken fibers. The fibers have been damaged during the preparation of the SEM specimen.

under an air atmosphere only (Figure S2).

From a number (n) = 100 Pd nanocrystals, the nanocrystal distribution shows a bimodal Pd-ANF distribution. A large number of small nanoparticles of ca 1.2 nm has been found after the reduction treatment, and a lower number of bigger particles (3.1, 3.2, and 4.8 nm for Pd1-ANF, Pd3-ANF, and Pd5-ANF). Additionally, the Pd3-ANF presents a high number of particles smaller than 3 nm. After CO oxidation, the nanocrystals' diameters widen, lowering the amount of small particles by ~1.2 and 1.7 nm. The results indicate that Pd nanocrystals might redistribute and form slightly larger particle sizes after CO oxidation (Fig. 2**b', 2d',** and **2f'**). Nanocrystal redistribution can be attributed to sintering[33,34]. A possible mechanism is that sintering occurs by removing smaller nanocrystals at the expense of even larger crystals[35, 36]. Despite the sintering, small nanocrystals remain present after the CO oxidation. A transversal SEM image from a broken nanofiber shows the presence of Pd NP inside the nanofiber when using SEM backscattered and secondary electrons (Figure S3). This indicates that adding metallic precursors while preparing the Al_2O_3 support generates a strong metal-support interaction (MSI), encapsulating and stabilizing Pd crystals [37,38].

Pd-ANFs (Fig. 2) are contrasted to Pd-ANPs (Figure S4) to evaluate the influence of the alumina morphology on the Pd nanocrystal's size. Similar sintering effects have been observed in the nanocrystal size distribution for Pd-ANPs. We observe for Pd1-ANF a slightly smaller nanocrystal size diameter than Pd1-ANP after H_2 reduction, which prevails after CO oxidation. After CO oxidation, Pd1-ANF and Pd1-ANP reveal similar nanocrystal sizes of 3.2 and 3.3 nm. Pd3-ANF, after H_2 reduction, has a significant number of 1.2 and 2.1 nm nanocrystals compared to Pd1-ANF. Compared to Pd3-ANP, a small number with 1.2 nm size has been found. Larger nanocrystals of 2.1 nm are observed in Pd3-ANP but not as pronounced as in Pd3-ANF. Nanocrystals of 3.2 nm have been found in both Pd3-ANF and Pd3-ANP. For CO oxidation in Figs. 2**d**-2**d'** and **S4d-S4d'**, larger nanocrystals have been observed for Pd3-ANP. To this end, no large variations have been observed for Pd5-ANF and Pd5-ANP.

The CO chemisorption is used to estimate the dispersion of the Pd-ANFs and Pd-NPs after their reduction in H_2 (Table 1). CO chemisorption increases when the Pd content is increased from 1 %w/w to 5 % w/w, either in Pd-ANF or Pd-ANP. From all samples, Pd3-ANF shows the highest dispersion. When we compare Pd3-ANF against Pd3-ANP, a drastic decrease in CO chemisorption is observed. A similar trend is observed when Pd5-ANF and Pd5-ANP are compared. Although slight S_{BET} variations between ANFs and NPs are observed in Table 1, differences can be considered negligible (~50 m^2/g). Our attributions are based on the S_{BET} representing the ANFs' and ANPs' internal surface area. For example, the external surface area associated with the fibers' geometry is smaller than the internal area and only adds a marginal increase to the S_{BET}. Please note that the diameter of the ANFs is around 200 nm; thus, the external surface area is insignificant. The ANFs are a better heterogeneous support for Pd crystals than their NPs counterpart.

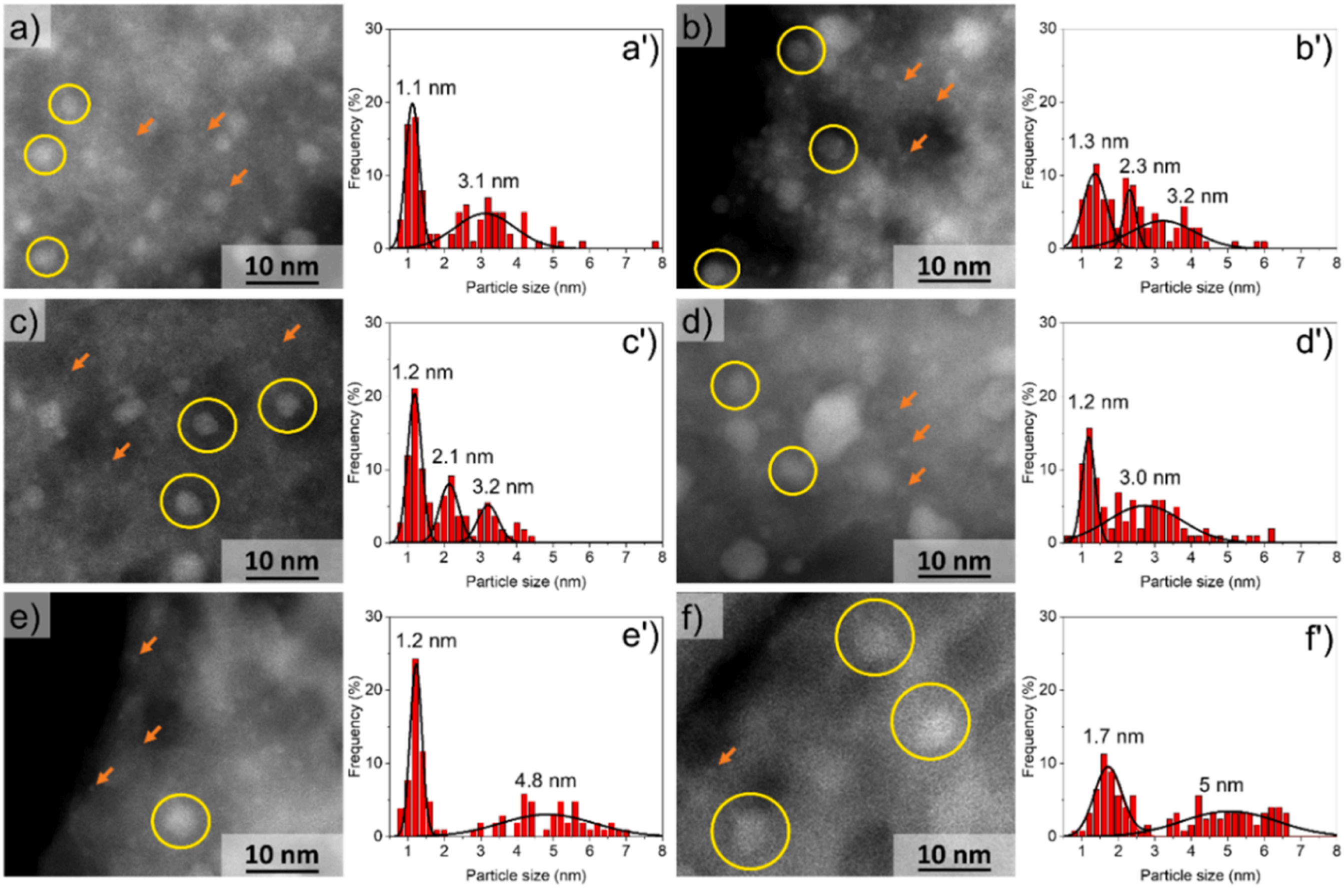

Fig. 2. STEM ADF images and Pd nanocrystal size distribution of (**a, a′**) Pd1-ANF, (**c, c′**) Pd3-ANF, and (**e, e′**) Pd5-ANF after CO adsorption. STEM ADF images and nanocrystal size distribution after CO oxidation are presented in (**b, b′**) Pd1-ANF, (**d, d′**) Pd3-ANF, and (**f, f′**) Pd5-ANF. Yellow open circles show Pd particles ~3.2–5 nm sizes, and orange arrows show the ~1.2 nm particles on the fibers.

Table 1

Textural, CO adsorption, surface Pd content by XPS, and TOF for Pd-ANFs and Pd-ANPs.

	S_{area} (m^2/g)	CO chemisorption (μmol/g)*	Particle diameter (nm)* *	Pd/Al Ex-situ XPS* **	TOF (s^{-1}) at 353 K
Pd1-ANF	207.7	26.1	2	0.01	0.052
Pd3-ANF	257.6	95	1.7	0.03	0.050
Pd5-ANF	220.8	95.1	2.8	0.05	0.050
Pd1-ANP	267.4	27.8	1.9	0.03	0.031
Pd3-ANP	250.8	59.1	2.7	0.06	0.029
Pd5-ANP	259.1	68.5	3.8	0.10	0.025

*CO chemisorption after H_2 reduction

**Calculated from the CO chemisorption experiment

* **Calculated from atomic % ratio, based on XPS areas

ANFs comprise a non-woven geometry facilitating CO to diffuse throughout their mesoscale network, promoting chemisorption, as shown in Table 1. Our attribution is evidenced in Figure S3, with pores inside the ANFs, which grants reactants contact with the encapsulated Pd crystals[9,10]. It should be noted that STEM ADF in Fig. 2 evidences the presence of single atoms and atom clusters. However, the particle size distribution of single atoms and clusters lower than < 1.2 nm is somewhat challenging to resolve unless it is used together with other spectroscopic techniques like EDX in Fig. 8. Hence, particle size distribution is not shown as it might require many particles to be revolved, e.g., n = 100.

3.2. *Active sites on Al_2O_3-supported Pd nanocrystals*

Understanding the active sites of Pd nanocrystals over mesoscopic architectures is a staircase toward connecting single atoms, clusters, and nanocrystals activity with processes occurring at larger scales. Pd activity can correlate to the type of active site in Pd. Therefore, IR spectroscopy of adsorbed CO (CO-IR) is assessed.

The non-H_2 reduced Pd3-ANFs and Pd3-ANPs' CO-IR spectra (i.e., primarily oxidized Pd over ANFs and ANPs) are benchmarked in Figure S5. After H_2 reduction, CO is adsorbed over the Pd-ANFs or Pd-ANPs (Fig. 3). For both catalysts, the spectra show IR signals of CO gas, possibly overlapping with a small IR band corresponding to linear CO-Pd^{2+}, as shown in Fig. 3, region 1 (**R1**). Region 2 (**R2**) is assigned to linear CO on Pd (Pd-CO_L), and Region 3 (**R3**) to multi-coordinated

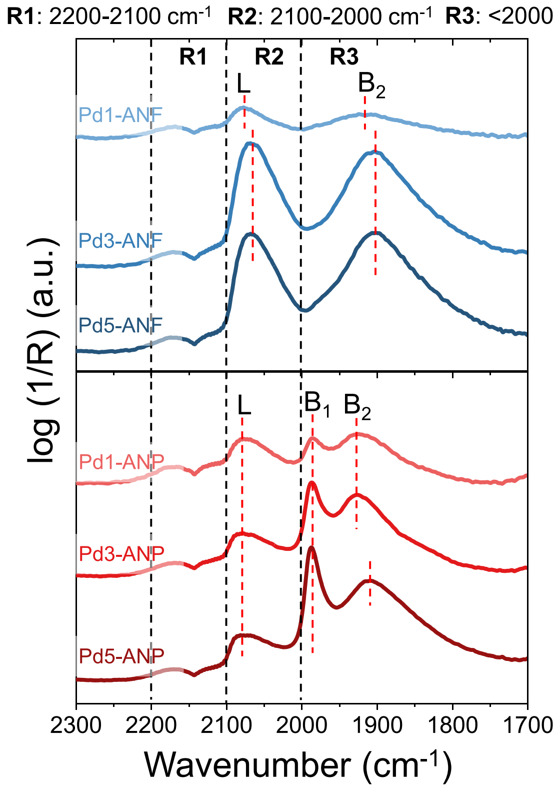

Fig. 3. CO-IR spectra after the exposure to 1 % CO on reduced Pd-ANFs and Pd-ANPs (**Point B**, Scheme 1).

bridge species (Pd-CO_B). In the case of Pd-ANP, three prominent IR bands at 2086 cm^{-1} (Pd-CO_L), 1985 cm^{-1} (Pd-CO_{B1}), and 1928 cm^{-1} (Pd-CO_{B2}) have been found. Pd-CO_{B1} is assigned to bi-coordinated CO on structurally open Pd nanocrystal planes, such as (100) or (210). IR bands around 1956 cm^{-1} (Pd-CO_{B2}) are ascribed to bi-coordinated CO on Pd (111) [39–41].

Compared to Pd1-ANPs in Fig. 3, Pd1-ANF possesses similar Pd-CO_L features. These features remain similar between higher ANF loading but with increased relative intensity for Pd-CO_L and Pd-CO_{B2}. In the case of Pd-CO_{B1}, no band has been observed in the Pd-ANFs. Similar to the Pd3-ANF and Pd5-ANF, relative intensity increases of the Pd-CO_{B2} band have been reported in the literature and attributed to a high metal fraction exposed in the catalyst, denoting the importance of ANF support properties and geometry. The development of the 1980–1995 cm^{-1} band (Pd-CO_{B1}) has also been attributed to low metal fractions[42,43]. Furthermore, the multiple CO bands in Fig. 3 appear due to a change in the exposed Pd facet[43–46]. The CO-IR results suggest that Pd (111) planes might be favored when Pd is supported in ANFs. STEM ADF images of Pd3-ANF in Fig. 4**a and** 4**b** support this hypothesis. The STEM results reveal that Pd is faceted, with Pd (111) planes dominating the nanocrystal morphology. At this point, the existence of Pd atoms cannot be confirmed with IR due to the heterogeneous system of Pd particles.

3.3. The chemical environment at the surface of Al_2O_3-supported Pd nanocrystals

Ex-situ XPS measurements have been carried out on air-annealed ANF and ANP loaded with Pd to understand the chemical environment. Figure S6 shows the Pd 3d spin-orbit coupling pair with two peaks corresponding to Pd $3d_{5/2}$ and Pd $3d_{3/2}$. For the fit, two doublets are assumed leading a Pd $3d_{5/2}$ peak at binding energy (BE) between 336.4 and 336.7 eV characteristic for Pd^{2+} in PdO [47,48] as well as between 338.2 and 339.0 eV, indicating the presence of PdO_2 species [48–50]. In general, great similarities can be found between the as-prepared Pd1-ANF, Pd3-ANF, and Pd5-ANF, which have more PdO_2 species. In contrast, Pd supported on ANP is mainly in the Pd^{2+} state with only minor PdO_2 present. Table 1 might help to shed light on this observation by looking at the Pd/Al ratio. Compared to the ANPs, the Pd/Al ratio is 1 order of magnitude lower for ANFs. Table 1 results indicate that ANPs

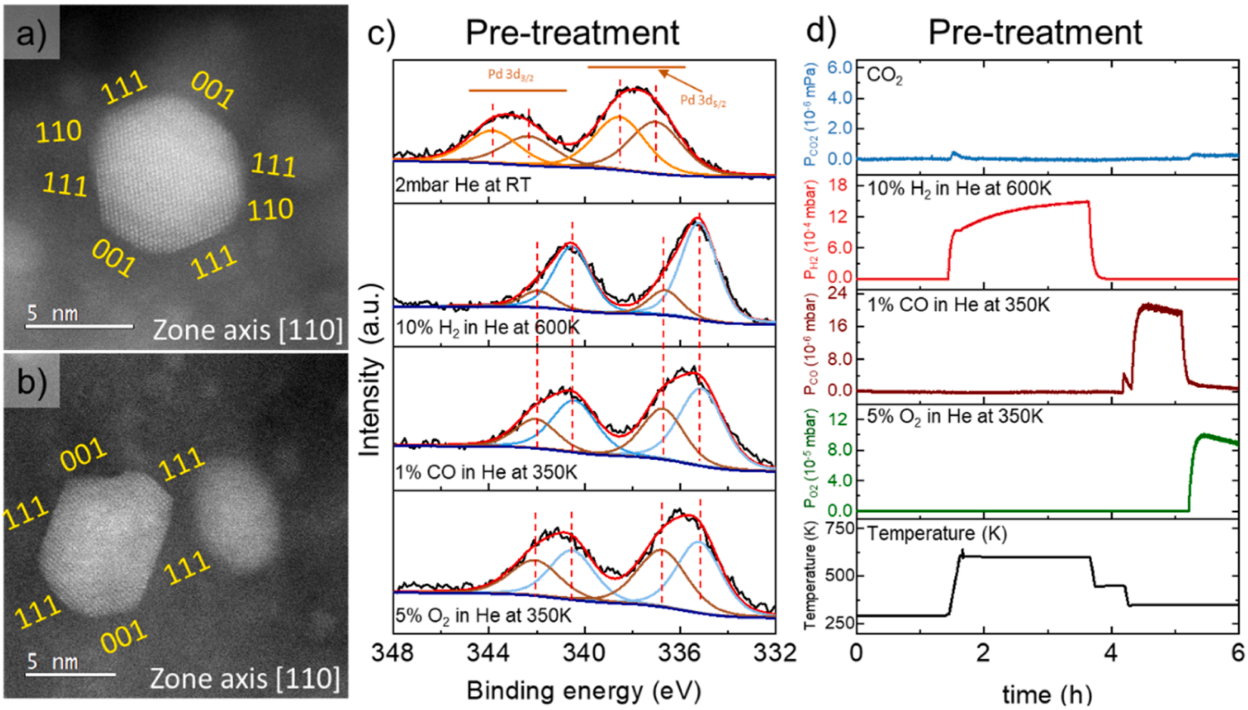

Fig. 4. (a-b) A close-up STEM ADF image of single Pd nanocrystals oriented in the [100] zone axis from Pd3-ANF. The Pd nanocrystal facets are colored yellow. NAP-XPS Pd 3d core spectra for Pd3-ANF during the pre-treatment (c) in various conditions (He, H_2, CO, and O_2) and (d) the MS data associated with each gas over time.

have more Pd exposed at the surface, which could prompt the formation of Pd^{2+} species. Furthermore, to explain the low Pd/Al ratios for ANFs, an SEM cross-section is shown in Figure S3. SEM results reveal the encapsulation of Pd crystals within the ANFs matrix, suggesting that a large portion of Pd is encapsulated within the ANFs.

Now, we focus on understanding the different chemical species in Pd nanocrystals under near-ambient pressure reaction conditions at a total pressure of 2 mbar. The pre-treatment and CO oxidation conditions at $\alpha_{CO} = 0.2$ are shown in Scheme 2 and have been chosen to be as similar as possible to the experimental conditions used for the IR-CO tests in Scheme 1**.** First, we start Pd3-ANF pre-treatment (Scheme 2). The Pd3-ANF has been selected among the other catalysts due to its highest CO oxidation characteristics. First, the as-prepared (known as air-annealed) Pd3-ANFs are analyzed in 2 mbar He at room temperature, see Fig. 4**c**. The two peaks in the Pd 3d region are fitted again with two doublets, assuming Pd^{2+} and Pd^{4+} (in PdO_2) are the oxidation states. However, comparing these results to the ex-situ measurements (Figure S6), it becomes evident that the relative amount of PdO_2 is even higher in the NAP-XPS data. A reason could be the preparation process with a mechanical press, which leads to breaking the ANFs apart and promoting more exposure to Pd NPs. In the next step, the sample is reduced to 10 % H_2 diluted in He at 600 K, leading to the appearance of a peak around 335.2 eV characteristic for Pd^0. Small amounts of Pd^{2+} can be found as well, thus indicating the formation of partially reduced Pd nanocrystals [51–54]. Cooling down to 350 K and changing the gas environment to 1 % CO leads to the decrease of Pd^0 and the increase of Pd^{+2} species. After that, we changed to 5 % O_2 diluted in He, maintaining the temperature at 350 K. The XPS analysis suggests that Pd nanocrystals are oxidized to Pd^{2+} again.

The NAP-XPS results are then correlated with mass spectrometry (MS), which is used to monitor the generation of CO_2 (Fig. 4**d**). In Fig. 4**d**, the MS data during the pre-treatment show a small amount of CO_2 generated during the reduction with H_2, possibly from carbonate species adsorbed on the catalyst. Interestingly, during the MS time course, CO_2 is generated when 1 % CO and 5 % O_2 pre-treatments are switched (~5 h in Fig. 4**d**). This indicates that after CO pre-treatment, CO remained adsorbed on the Pd, reacting with O_2 to form small amounts of CO_2.

Fig. 5 demonstrates the changes in the Pd oxidation states over various temperatures at $\alpha_{CO} = 0.2$. In Fig. 5**a** ($\alpha_{CO} = 0.2$ at 350 K), we observe a mixture of Pd^{2+} and PdO_2 species[51–54], which remains present across temperatures ranging from 350 to 600 K. The results are then compared with the recorded data from MS in Fig. 5**b**. The results evidenced that CO_2 formation starts around 350 K. As the temperature increases to 550 K, the highest CO_2 amount has been found. Higher temperatures than 550 K do not necessarily lead to an increase in the CO_2 content. No variations for the Pd oxidation state between $\alpha_{CO} = 0.1$, 0.2, and 0.3 are expected for the various ANF and NP loadings. However, discussing the reaction performance is essential for the multiple catalysts. The results are presented in the section below.

3.4. Light-off curves of Al_2O_3-supported Pd nanocrystals

The catalytic performance of the Pd-ANFs and Pd-ANPs for CO oxidation demonstrates the importance of controlling the Pd species in ANFs. In this experiment, we use three α_{CO} values ($\alpha_{CO} = 0.1$, 0.2, and 0.5) described in Scheme 1. The light-off results are shown in Fig. 6, and it should be noted that they agree with NAP-XPS findings in Fig. 5, where CO starts oxidizing around 350 K. Light-off curves for CO oxidation for Pd1-ANF, Pd3-ANF, and Pd5-ANF are shown in Fig. 6**a-c**. Light-off curves for Pd1-ANP, Pd3-ANP, and Pd5-ANP are shown in Fig. 6**d-f**. It is worth mentioning that at low conversions ($\alpha_{CO} = 0.1$), the S/N ratio is too low and causes a very noisy baseline.

A common feature for $\alpha_{CO} = 0.5$ in Fig. 6 is that temperatures higher

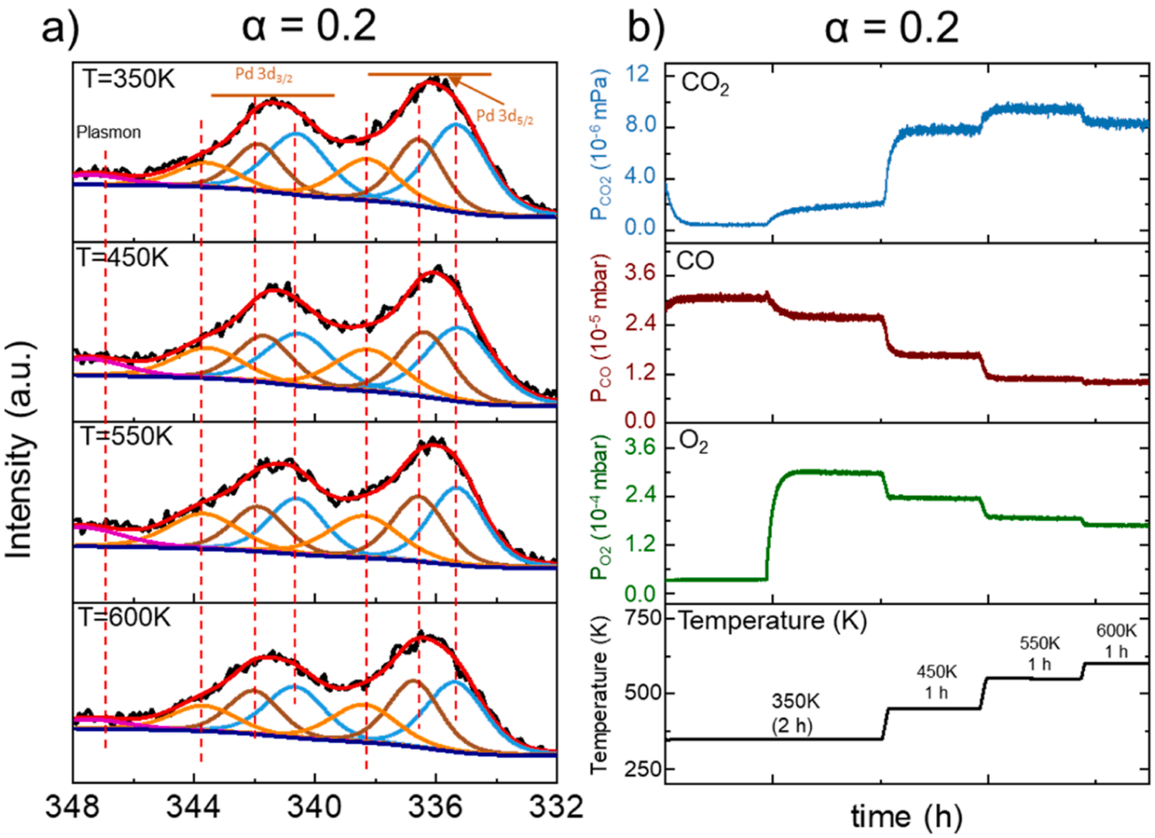

Fig. 5. (a) NAP-XPS Pd 3d core spectra for Pd3-ANF after the pre-treatment at $\alpha_{CO} = 0.2$ over various temperatures and (b) the associated MS data during the CO reaction.

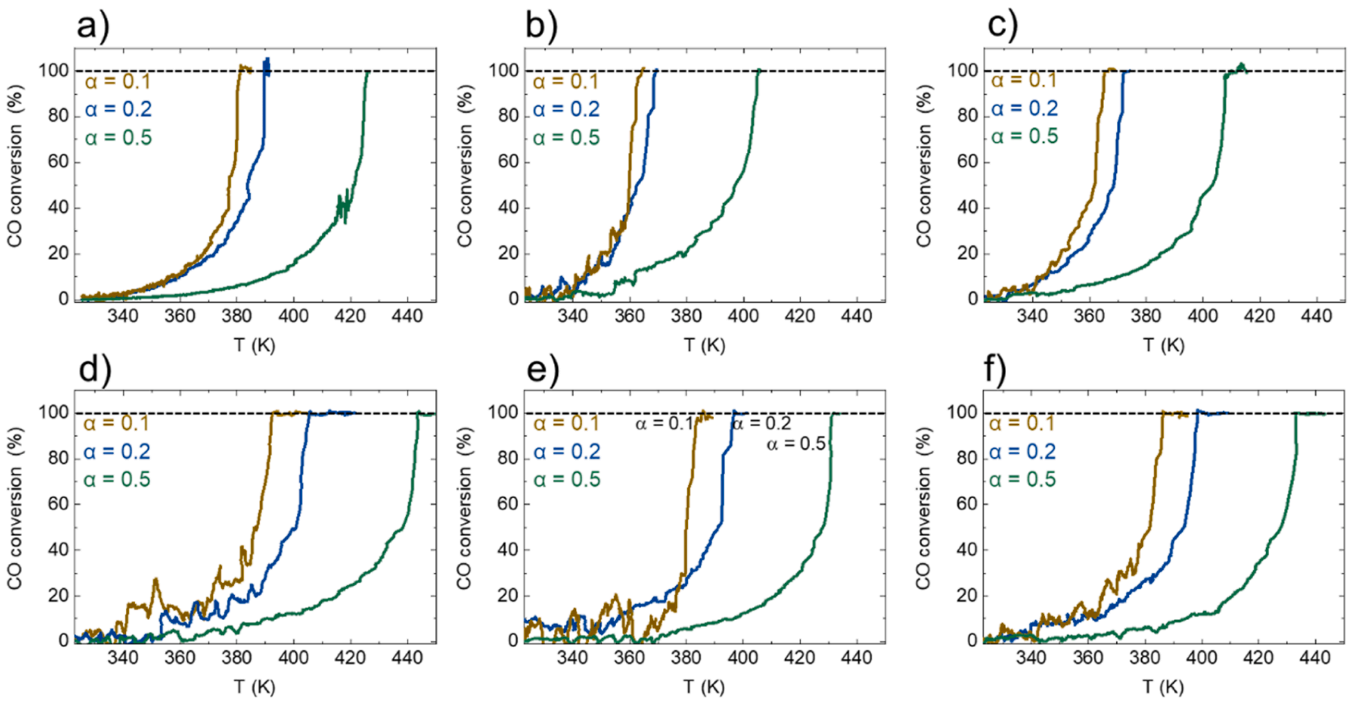

Fig. 6. Light-off curves during CO oxidation at various α_{CO} ratios (0.1, 0.2, 0.5) for (**a**) Pd1-ANF, (**b**) Pd3-ANF, (**c**) Pd5-ANF, (**d**) Pd1-ANP, (**e**) Pd3-ANP, and (**f**) Pd5-ANP.

than 393 K are required to oxidize CO. This is a known phenomenon since the CO surface reaction depends on the CO and O_2 coverage. At higher CO coverages, CO blocks O_2 to adsorb (possibly poisoning), hindering oxidation[40,55]. For other alpha values (i.e., $\alpha_{CO} = 0.1$ and 0.2), the light-off curve shows that a lower temperature is required to oxidize CO to CO_2. Within this set of experiments, $\alpha_{CO} = 0.1$ shows the lowest oxidation temperature. The Pd-ANFs have a light-off onset of around 353 K, 20 K lower than Pd-ANPs.

T_{50} has been obtained from Fig. 6 and is shown in Fig. 7 for a direct comparison. In Fig. 7, T_{50} is plotted against α_{CO}, where we observed that Pd-ANFs have lower reaction temperatures than Pd-ANPs counterparts, indicating that (i) the Pd chemical environment and (ii) the ANF structure can aid, in general, chemical reaction outperformance. It should be noted that compared to the highly loaded catalysts, Pd1-ANF and Pd1-ANP required a higher temperature for CO to oxidize.

The turnover frequency (TOF) values are calculated for Pd-ANFs and Pd-ANPs. Table 1 presents the TOF at 353 K and α_{CO}= 0.1, which were ca. 0.05 s^{-1} for the Pd-ANF and 0.03 s^{-1} for the Pd-ANP, respectively. Fig. 8 shows the tendency of all Pd-ANFs and Pd-ANPs. These results confirm that Pd-ANFs exhibit higher catalytic activity due to (i) the unique structural properties of the nanofibers, including a small length-to-diameter (L/D) ratio, high surface area, and optimized pore distribution, which enhances diffusion; (ii) the higher Pd dispersion, which increases the CO reaction rate by exposing more active Pd atoms; and (iii) the distinct chemical environment of Pd nanoparticles, as revealed by XPS and CO-IR analyses.

We can then connect the results from Figs. 6–8 with CO chemisorption in Table 1. The Pd-ANFs are more active for CO chemisorption. Higher dispersion indicates higher catalytic activity, which agrees with

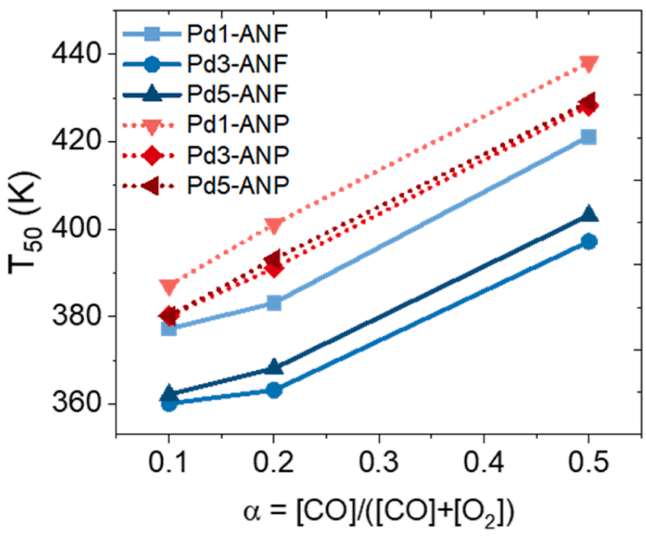

Fig. 7. T_{50} as a function of α_{CO} for Pd-ANFs and Pd-ANPs.

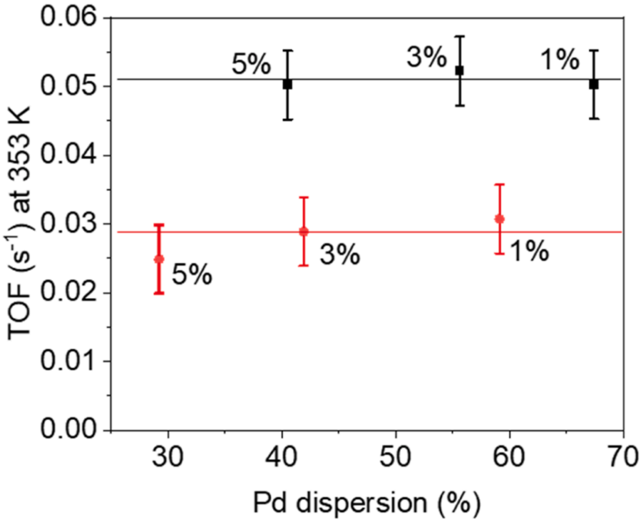

Fig. 8. TOF as a function of Pd dispersion for Pd-ANFs (black) and Pd-ANPs (red) loaded with 1 % wt., 3 % wt., and 5 % wt.

Figs. 7 and 8. These demonstrate the functionality of structuring the materials, particularly in the ANF shape. Structured catalysts can improve the accessibility to active sites and help increase the catalytic activity[56]. In the case of nanofibers, higher performance is attributed to the stabilization of Pd species, as it could be prone to PdO_2. It is also proposed that the specific fiber stacking increases diffusivity and reduces transport limitations [56–59]. Although these experiments have been carried out under a kinetic control regime, the nanofiber structure can help to reduce the mass and heat transfer limitations in more demanding reactions in two ways: (i) the low particle (nanofiber) diameter and thus the high length/diameter ratio, reduces the internal transport limitations, while (ii) the open space between the nanofibers creates pores high enough to enhance the transport processes. To this end, it is important to understand the reaction mechanism behind the experimental light-off curves. The mechanism is discussed in the next section.

The XPS and CO-IR results also revealed significant differences in Pd nanoparticles' electronic state and surface chemistry. XPS analysis indicated a stronger metal-support interaction (MSI) when Pd is supported on the nanofibers. The CO-IR results showed that Pd-ANFs exhibit a higher fraction of Pd-CO_L than Pd-ANPs, which presents a more significant amount of Pd-CO_B. This suggests that Pd-NFs likely contain a higher proportion of isolated Pd atoms and small Pd clusters, which facilitate O_2 activation and mitigate CO poisoning, thereby enhancing catalytic performance.

3.5. Mechanistic insights: light-off

Experimentally, the importance of Pd nanocrystals over mesoscopic architectures, like ANFs, has been demonstrated, and understanding helps us connect catalyst structures with activity. Hence, it is important to understand the role of Pd species during light-off mechanistically. Therefore, existing predictive *ab initio* kinetic models have been implemented for Pd(111), Pd(110), Pd(100), and Pd single atoms adsorbed/supported on Al_2O_3 (see Supporting Information **Sections 7** and **8** and Table S2, Figures S7-S10 for computational and kinetic modeling details).

Our models have been evaluated in the same temperature window (250–450 K) for different α_{CO} (Fig. 9). The light-off curves are simulated for *ab initio* kinetic models of various molecular systems; the pristine low index Pd surfaces Pd(111), Pd(110), Pd(100), and Pd single atoms adsorbed on Al_2O_3. Interestingly, the light-off order for these model systems follows the same trend, *i.e.*, $\alpha_{0.5} < \alpha_{0.2} < \alpha_{0.1}$, in order of increasing light-off temperature (Figure S9, Fig. 9h), which is the opposite of the order depicted experimentally (Figs. 6 and 7).

The key factor playing an essential role in the experimental light-off

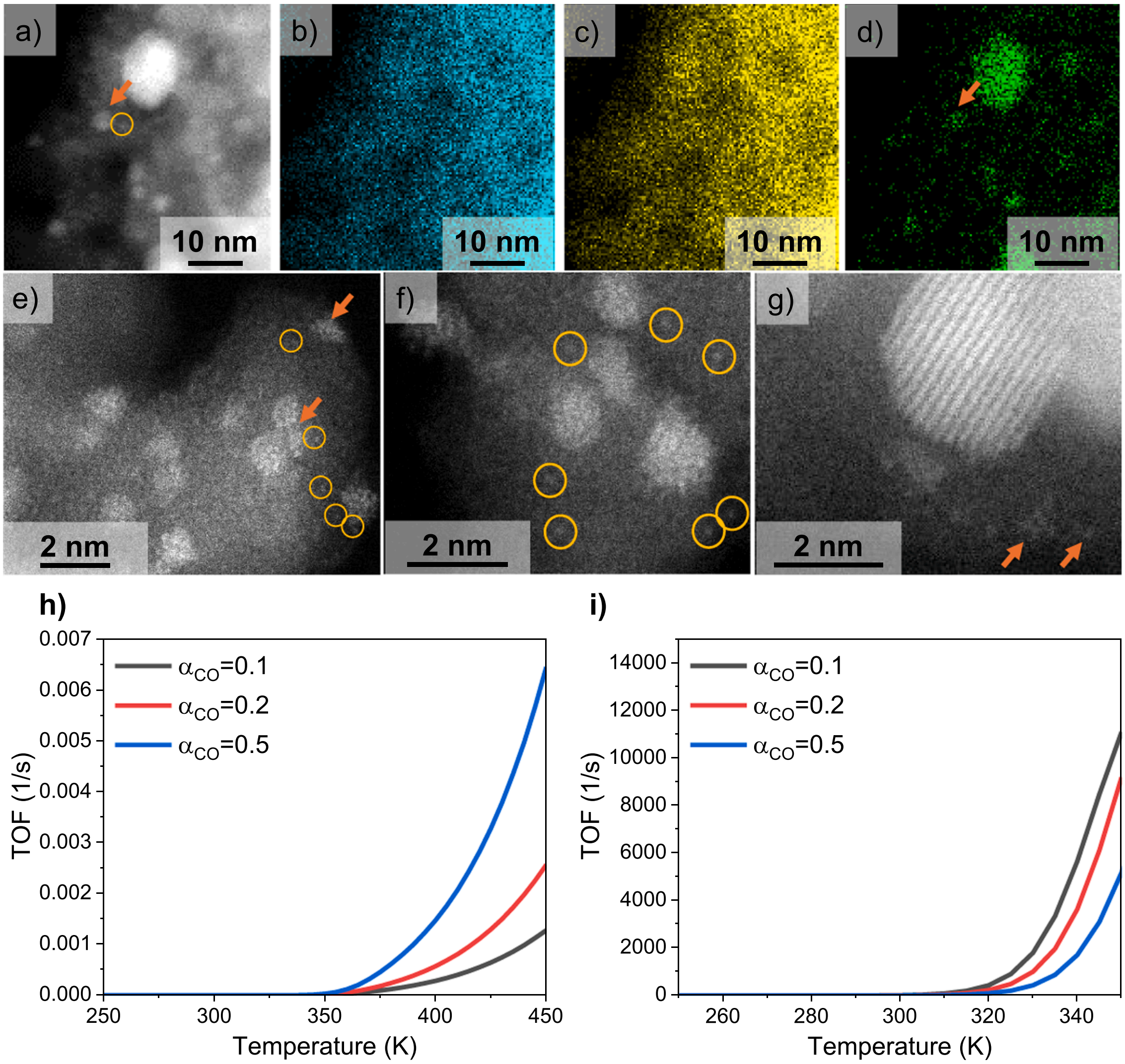

Fig. 9. (a-d) ADF and STEM-EDXS map for (b) oxygen (light blue), (c) aluminum (yellow), and Pd (green). (e) Pd3-ANF after the reduction step and (f-g) after the CO oxidation cycle steps. (h) Simulated light-off curves as a function of α_{CO} for Pd/Al_2O_3 for the Alexopoulos kinetic model[63] and (i) the modified kinetic model. Open yellow circles are assigned to Pd atoms, and arrows are assigned to slightly larger crystals.

behavior (Figs. 6 and 7) is the existence of Pd single atoms, which are clearly observed experimentally with STEM ADF (see Figs. 9**a**-9**g**). STEM-EDXS reveals the chemical composition of the Pd3-ANF (Scheme 1, **step A**). Pd3-ANF is composed of oxygen (light blue), aluminum (yellow), and Pd (green), as shown in Figs. 9a-9**d**. Pd clusters have been observed in the STEM-EDXS maps, indicating the presence of small particles (orange arrows). Remarkably, Pd atoms have been observed after the reduction reaction (Scheme 1, **step A**), as shown in Fig. 9**e** (yellow open circles), which prevailed after CO oxidation (Figure Scheme 1, **step C**). After the CO oxidation reaction, the STEM ADF results provide additional support for the co-existence of Pd atoms, clusters, and nanocrystals over the ANFs (Figs. 9**f**-9**g**, yellow open circles, and orange arrows).

The presence of Pd as single atoms in ANFs is crucial since it can help maximize the efficiency of metal atom use and enable high activity and selectivity during reaction [60–62], such as temperature reduction during light-off (Figs. 6 and 7). Herein, it is shown that using *ab initio* kinetic modeling Pd single-atoms is necessary to explain the light-off trends. Our model plots surface coverages for an original kinetic model for CO oxidation on Pd single atoms adsorbed on Al_2O_3 with different values of α (Figure S10). We remark that below 340 K, at temperatures before the experimental light-off starts, it is clear that the dominant species are in decreasing order of abundance 2CO*PdO$_2$/Al_2O_3, 2CO*Pd/Al_2O_3, and CO*Pd/Al_2O_3 (Figure S10a-**c**); nevertheless, the qualitative light-off trends for different α remain the same as on the low-index Pd surfaces. However, suppose we imagine that the abundant species can react with each other. In that case, the probability that these species become neighbors in the kinetic model can be statistically determined by multiplying both coverages and their reaction probability by calculating the activation barriers for the first and second CO oxidation (Figure S8).

We proceed then to extend the Alexopoulos kinetic model [63] (Fig. 9**h**) with a 16th reaction featuring CO oxidation by abundant Pd-single atoms species coupling of neighboring (see Table S2), yielding a revised kinetic model for which the light-off temperatures increase with increasing α_{CO} (Fig. 9**i**). The results align with Fig. 6 experimental data and allow us to understand why the light-off temperature is typically below 400 K (Figs. 6 and 7), which does not happen on pure low-index Pd facets (Figure S9) nor Pd nanoparticles at such low temperatures. Experimentally, the picture is somehow complex as both single atoms and nanoparticles are present (Fig. 2, Fig. 4, and Fig. 9). While it is nearly impossible to construct *ab initio* kinetic models accounting for a whole active site distribution of supported Pd single atoms and Pd nanoparticles (Fig. 2), it is nevertheless possible, thanks to our *ab initio* kinetic modeling results (Figure S10) to unravel the importance and role of Pd single atoms to start the CO-oxidation light-off at temperatures below 373 K when Pd-nanoparticles and Pd-facets are still CO-poisoned. Furthermore, subsequent translation of CO molecules from Pd nanoparticles to Pd single atoms could allow these single atoms to be replenished with CO molecules. Finally, because Pd single atoms can be readily oxidized without CO poisoning, the Mars-Van Krevelen reaction mechanism will thrive at these low temperatures, as observed for other oxide/metal interfaces [64].

4. Conclusions

ANFs containing Pd nanoparticles have been synthesized using electrospinning, and their chemical surface has subsequently been analyzed. Analysis of the chemical surface revealed different Pd chemical species. STEM ADF reveals Pd particles are highly dispersed in the Pd loaded alumina nanofibers (Pd-ANF), compared to the Pd loaded alumina nanoparticles (Pd-ANP), while an infrared analysis of adsorbed CO on both types of catalyst helps to identify various CO adsorption sites over the catalysts.

More in particular, the CO-IR spectra of Pd-ANFs and Pd-ANPs after H_2 reduction reveal the presence of CO adsorbed in Pd (CO-L_I, CO-L_{II}, CO-B_2), while the presence of CO-B_1 adsorption site is only present in Pd-ANPs. The absence of CO-B_1 sites is attributed to smaller Pd particle sizes and higher chemisorption in Pd-ANFs. Furthermore, CO oxidation experiments also pointed to the advantage of Pd-ANFs over Pd-ANPs, contributing to a decrease in the light-off temperature, most probably due to the higher dispersion of Pd nanoparticles and Pd single atoms in the more structured ANF catalysts, which is another indication of the higher intrinsic activity of smaller Pd nanoparticles and their stronger metal support interactions. Light-off curves based on *ab initio* kinetic models on different molecular systems, such as pristine low index Pd surfaces and Pd single atoms adsorbed on Al_2O_3, shade light on the underlying light-off mechanisms. An amendment to an existing kinetic model on Pd single atoms by including a CO oxidation reaction between abundant single-atom species can explain the experimentally observed low light-off temperatures for the different CO/O_2 ratios.

CRediT authorship contribution statement

Ruiz-Zepeda F.: Writing – original draft, Visualization, Funding acquisition, Formal analysis, Data curation. **Cazac D.:** Writing – original draft, Investigation, Data curation. **Susarrey-Arce Arturo:** Writing – review & editing, Writing – original draft, Supervision, Investigation, Conceptualization. **Rodriguez-Olguin M.A.:** Writing – review & editing, Writing – original draft, Visualization, Validation, Investigation, Formal analysis, Data curation, Conceptualization. **Gardeniers J.G.E.:** Writing – review & editing, Writing – original draft, Supervision, Project administration, Funding acquisition. **Aguirre A.:** Writing – review & editing, Writing – original draft, Visualization, Validation, Supervision, Investigation, Funding acquisition, Formal analysis, Data curation, Conceptualization. **Vandichel M.:** Writing – review & editing, Writing – original draft, Visualization, Validation, Investigation, Funding acquisition, Formal analysis, Conceptualization. **Manzo-Robledo A.:** Writing – review & editing, Writing – original draft, Investigation. **Eckelt R.:** Investigation, Formal analysis, Data curation. **Atia H.:** Methodology, Investigation, Formal analysis, Data curation. **Bosco M.:** Investigation, Formal analysis, Data curation. **Bartling S.:** Validation, Supervision, Methodology, Investigation, Formal analysis, Data curation.

Declaration of Competing Interest

We wish to confirm that there are no known conflicts of interest associated with this publication, and there has been no significant financial support for this work that could have influenced its outcome.

Acknowledgments

The authors thank Mark Smithers (MESA+ Institute, University of Twente) for his support. The research leading to the results in this report has received funding from the European Research Council (ERC) under the European Union's Horizon 2020 research and innovation program (Grant Agreement No. 742004). The authors are also grateful for the financial support from the Agencia Nacional de Promoción de la Investigación, el Desarrollo Tecnológico y la Innovación (ANPCyT) [Grant No. PICT-2020-03411]. M.V. acknowledges funding from the European Union's Horizon 2020 research and innovation program (HERMES, grant agreement Nr. 952184), Research Ireland (MEM-E-TECH, 23/FFP-A/12221), and support of the Irish Centre for High-End Computing (ICHEC) for the provision of computational facilities. F.R.-Z. acknowledges the European Research Council (ERC), for the ERC starting Grant 123STABLE (grant agreement ID: 852208).

Appendix A. Supporting information

Supplementary data associated with this article can be found in the online version at doi:10.1016/j.mtcata.2025.100093.

References

[1] I. Levin, D. Brandon, Metastable alumina polymorphs: crystal structures and transition sequences, J. Am. Ceram. Soc. 81 (1998) 1995–2012, https://doi.org/10.1111/j.1151-2916.1998.tb02581.x.

[2] G. Busca, The surface of transitional aluminas: a critical review, Catal. Today 226 (2014) 2–13, https://doi.org/10.1016/j.cattod.2013.08.003.

[3] Z. Yu, C. Guo, X. Pang, Y. Shen, M. Gao, S. Zhao, Y. Wang, G. Luo, Coprecipitation synthesis of large-pore-volume γ-alumina nanofibers by two serial membrane dispersion microreactors with a circulating continuous phase, Ind. Eng. Chem. Res. 62 (2022) 1415–1424, https://doi.org/10.1021/acs.iecr.2c03920.

[4] Y. Wang, Z. Li, W. Fu, Y. Sun, Y. Dai, Core–Sheath CeO2/SiO2 nanofibers as nanoreactors for stabilizing sinter-resistant Pt, enhanced catalytic oxidation and water remediation, Adv. Fiber Mater. 4 (2022) 1278–1289, https://doi.org/10.1007/s42765-022-00177-0.

[5] M. Tang, S. Liu, W. Fu, J. Wang, K. Yin, M. Zhu, J. Tian, Y. Sun, Y. Dai, Surface oxygen vacancies promoted Pt nanoparticles on celery-like CeO2 nanofibers for enhanced sinter-resistance and catalytic performance, Mater. Today Nano 20 (2022) 100249, https://doi.org/10.1016/j.mtnano.2022.100249.

[6] C. Márquez-Alvarez, N. Žilková, J. Pérez-Pariente, J. Čejka, Synthesis, characterization and catalytic applications of organized mesoporous aluminas, Catal. Rev. Sci. Eng. 50 (2008) 222–286, https://doi.org/10.1080/01614940701804042.

[7] H. Liu, X. Liu, J. Yu, Y.T. Liu, B. Ding, Recent progress in electrospun Al2O3 nanofibers: component design, structure regulation and performance optimization, Appl. Mater. Today 29 (2022) 101675, https://doi.org/10.1016/j.apmt.2022.101675.

[8] B. Dhokale, A. Susarrey-Arce, A. Pekkari, A. Runemark, K. Moth-Poulsen, C. Langhammer, H. Härelind, M. Busch, M. Vandichel, H. Sundén, Microwave-heated γ-alumina applied to the reduction of aldehydes to alcohols, ChemCatChem 12 (2020) 6344–6355, https://doi.org/10.1002/cctc.202001284.

[9] M.A. Rodriguez-Olguin, H. Atia, M. Bosco, A. Aguirre, R. Eckelt, E.D. Asuquo, M. Vandichel, J.G.E. Gardeniers, A. Susarrey-Arce, Al2O3 nanofibers prepared from aluminum Di(sec-butoxide)acetoacetic ester chelate exhibits high surface area and acidity, J. Catal. 405 (2022) 520–533, https://doi.org/10.1016/j.jcat.2021.11.019.

[10] M.A. Rodriguez-Olguin, R.N. Cruz-Herbert, H. Atia, M. Bosco, E.L. Fornero, R. Eckelt, D.A. de Haro Del Río, A. Aguirre, J.G.E. Gardeniers, A. Susarrey-Arce, Tuning the catalytic acidity in Al2O3 nanofibers with mordenite nanocrystals for dehydration reactions, Catal. Sci. Technol. 12 (2022) 4243–4254, https://doi.org/10.1039/d2cy00143h.

[11] W. Fu, Y. Dai, J.P.H. Li, Z. Liu, Y. Yang, Y. Sun, Y. Huang, R. Ma, L. Zhang, Y. Sun, Unusual hollow Al2O3 nanofibers with loofah-like skins: intriguing catalyst supports for thermal stabilization of Pt nanocrystals, ACS Appl. Mater. Interfaces 9 (2017) 21258–21266, https://doi.org/10.1021/acsami.7b04196.

[12] F. Schüth, K.S.W. Sing, J. Weitkamp, Handbook of Porous Solids (eds.), Wiley, 2002, https://doi.org/10.1002/9783527618286.

[13] J.L. Williams, Monolith structures, materials, properties and uses, Catal. Today 69 (2001) 3–9, https://doi.org/10.1016/S0920-5861(01)00348-0.

[14] C. Parra-Cabrera, C. Achille, S. Kuhn, R. Ameloot, 3D printing in chemical engineering and catalytic technology: structured catalysts, mixers and reactors, Chem. Soc. Rev. 47 (2018) 209–230, https://doi.org/10.1039/c7cs00631d.

[15] C. Weidmann, K. Brezesinski, C. Suchomski, K. Tropp, N. Grosser, J. Haetge, B. M. Smarsly, T. Brezesinski, Morphology-controlled synthesis of nanocrystalline η-Al 2O 3 thin films, powders, microbeads, and nanofibers with tunable pore sizes from preformed oligomeric oxo-hydroxo building blocks, Chem. Mater. 24 (2012) 486–494, https://doi.org/10.1021/cm202692q.

[16] J. Winczewski, M.H. Zaldívar, H.J.G.E. Gardeniers, A. Susarrey-Arce, White emission in 3D-printed phosphor microstructures, Chem. Commun. (2023), https://doi.org/10.1039/D2CC06953A.

[17] J. Winczewski, M. Herrera, C. Cabriel, I. Izeddin, S. Gabel, B. Merle, A. Susarrey Arce, H. Gardeniers, Additive manufacturing of 3D luminescent ZrO2:Eu3+ architectures, Adv. Opt. Mater. 10 (2022) 2102758, https://doi.org/10.1002/adom.202102758.

[18] J. Winczewski, M. Herrera, H. Gardeniers, A. Susarrey-Arce, White emission in 3D-printed phosphor microstructures, Chem. Commun. 59 (2023) 3095–3098, https://doi.org/10.1039/D2CC06953A.

[19] C. Hurt, M. Brandt, S.S. Priya, T. Bhatelia, J. Patel, P.R. Selvakannan, S. Bhargava, Combining additive manufacturing and catalysis: a review, Catal. Sci. Technol. 7 (2017) 3421–3439, https://doi.org/10.1039/C7CY00615B.

[20] J.P. Winczewski, J. Arriaga-Dávila, C. Rosero-Arias, A. Susarrey-Arce, Tailoring chemistry for inorganic 3D micro-optics, Trends Chem. 6 (2024) 58–61, https://doi.org/10.1016/j.trechm.2023.12.005.

[21] C. Eyovge, C.S. Deenen, F. Ruiz-Zepeda, S. Bartling, Y. Smirnov, M. Morales-Masis, A. Susarrey-Arce, H. Gardeniers, Color tuning of electrochromic TiO2nanofibrous layers loaded with metal and metal oxide nanoparticles for smart colored windows, ACS Appl. Nano Mater. 4 (2021) 8600–8610, https://doi.org/10.1021/ACSANM.1C02231.

[22] K. Eid, M.H. Sliem, A.S. Eldesoky, H. Al-Kandari, A.M. Abdullah, Rational synthesis of one-dimensional carbon nitride-based nanofibers atomically doped with Au/Pd for efficient carbon monoxide oxidation, Int. J. Hydrog. Energy 44 (2019) 17943–17953, https://doi.org/10.1016/J.IJHYDENE.2019.05.105.

[23] X. Du, W. Han, Z. Tang, J. Zhang, Controlled synthesis of Pd/CoOx–InOx nanofibers for low-temperature CO oxidation reaction, N. J. Chem. 43 (2019) 14872–14882, https://doi.org/10.1039/C9NJ03055G.

[24] K. Eid, M.H. Sliem, H. Al-Kandari, M.A. Sharaf, A.M. Abdullah, Rational synthesis of porous graphitic-like carbon nitride nanotubes codoped with Au and Pd as an efficient catalyst for carbon monoxide oxidation, Langmuir 35 (2019) 3421–3431, https://doi.org/10.1021/ACS.LANGMUIR.8B03588.

[25] X. Du, F. Dong, Z. Tang, J. Zhang, The synthesis of hollow In2O3 @ Pd-Co3O4 core/shell nanofibers with ultra-thin shell for the low-temperature CO oxidation reaction, Appl. Surf. Sci. 505 (2020) 144471, https://doi.org/10.1016/J.APSUSC.2019.144471.

[26] J. Wang, H. Chen, Z. Hu, M. Yao, Y. Li, A review on the Pd-based three-way catalyst, Catal. Rev. Sci. Eng. 57 (2015) 79–144, https://doi.org/10.1080/01614940.2014.977059.

[27] C. Márquez-Alvarez, N. Žilková, J. Pérez-Pariente, J. Čejka, Synthesis, characterization and catalytic applications of organized mesoporous aluminas, Catal. Rev. Sci. Eng. 50 (2008) 222–286, https://doi.org/10.1080/01614940701804042.

[28] R.J. Liu, P.A. Crozier, C.M. Smith, D.A. Hucul, J. Blackson, G. Salaita, Metal sintering mechanisms and regeneration of palladium/alumina hydrogenation catalysts, Appl. Catal. A Gen. 282 (2005) 111–121, https://doi.org/10.1016/j.apcata.2004.12.015.

[29] J.R. Gaudet, A. de La Riva, E.J. Peterson, T. Bolin, A.K. Datye, Improved low-temperature CO oxidation performance of Pd supported on la-stabilized alumina, ACS Catal. 3 (2013) 846–855, https://doi.org/10.1021/cs400024u.

[30] O.H. Laguna, P.F. Lietor, F.J.I. Godino, F.A. Corpas-Iglesias, A review on additive manufacturing and materials for catalytic applications: milestones, key concepts, advances and perspectives, Mater. Des. 208 (2021) 109927, https://doi.org/10.1016/j.matdes.2021.109927.

[31] A. Susarrey-Arce, M.A. Hernández-Espinosa, F. Rojas-González, C. Reed, V. Petranovskii, A. Licea, Inception and trapping of ZnO nanoparticles within desilicated mordenite and ZSM-5 zeolites, Part. Part. Syst. Charact. 27 (2010) 100–111, https://doi.org/10.1002/ppsc.201000027.

[32] A. Aguirre, S.E. Collins, Design of an optimized DRIFT cell/microreactor for spectrokinetic investigations of surface reaction mechanisms, Mol. Catal. 481 (2020) 100628, https://doi.org/10.1016/j.mcat.2018.07.003.

[33] A. Pekkari, Z. Say, A. Susarrey-Arce, C. Langhammer, H. Härelind, V. Sebastian, K. Moth-Poulsen, Continuous Microfluidic Synthesis of Pd Nanocubes and PdPt Core-Shell Nanoparticles and Their Catalysis of NO2 Reduction, ACS Appl. Mater. Interfaces 11 (2019) 36196–36204, https://doi.org/10.1021/acsami.9b09701.

[34] A. Susarrey-Arce, R.M. Tiggelaar, J.G.E. Gardeniers, A. Van Houselt, L. Lefferts, CO Adsorption on Pt nanoparticles in low E-fields studied by ATR-IR spectroscopy in a microreactor, J. Phys. Chem. C 119 (2015) 24887–24894, https://doi.org/10.1021/acs.jpcc.5b08392.

[35] J.J. Chen, E. Ruckenstein, Sintering of palladium on alumina model catalyst in a hydrogen atmosphere, J. Catal. 69 (1981) 254–273, https://doi.org/10.1016/0021-9517(81)90163-9.

[36] S.B. Simonsen, I. Chorkendorff, S. Dahl, M. Skoglundh, S. Helveg, Coarsening of Pd nanoparticles in an oxidizing atmosphere studied by in situ TEM, Surf. Sci. 648 (2016) 278–283, https://doi.org/10.1016/j.susc.2015.11.003.

[37] J. Lin, X. Chen, Y. Zheng, F. Huang, Y. Xiao, Y. Zheng, L. Jiang, Facile construction of ultrastable alumina anchored palladium catalysts via a designed one pot strategy for enhanced methane oxidation, Catal. Sci. Technol. 10 (2020) 4612–4623, https://doi.org/10.1039/D0CY00727G.

[38] E. Yuan, C. Wu, G. Liu, L. Wang, One-pot synthesis of Pd nanoparticles on ordered mesoporous Al2O3 for catalytic hydrogenation of 2-ethyl-anthraquinone, Appl. Catal. A Gen. 525 (2016) 119–127, https://doi.org/10.1016/J.APCATA.2016.07.015.

[39] Y. Zhang, Y. Cai, Y. Guo, H. Wang, L. Wang, Y. Lou, Y. Guo, G. Lu, Y. Wang, The effects of the Pd chemical state on the activity of Pd/Al2O3 catalysts in CO oxidation, Catal. Sci. Technol. 4 (2014) 3973–3980, https://doi.org/10.1039/c4cy00552j.

[40] J.R. Gaudet, A. de la Riva, E.J. Peterson, T. Bolin, A.K. Datye, Improved low-temperature CO oxidation performance of Pd supported on La-stabilized alumina, ACS Catal. 3 (2013) 846–855, https://doi.org/10.1021/cs400024u.

[41] A. Bensalem, J.C. Muller, D. Tessier, F. Bozon-Verduraz, Spectroscopic study of CO adsorption on palladium-ceria catalysts, J. Chem. Soc. - Faraday Trans. 92 (1996) 3233–3237, https://doi.org/10.1039/FT9969203233.

[42] D. Tessier, A. Rakai, F. Bozon-Verduraz, Spectroscopic study of the interaction of carbon monoxide with cationic and metallic palladium in palladium-alumina catalysts, J. Chem. Soc. Faraday Trans. 88 (1992) 741–749, https://doi.org/10.1039/FT9928800741.

[43] R.F. Hicks, H. Qi, M.L. Young, R.G. Lee, Structure Sensitivity of Methane Oxidation over Platinum and Palladium, 1990.

[44] J. Oh, H.B. Bathula, J.H. Park, Y.W. Suh, A sustainable mesoporous palladium-alumina catalyst for efficient hydrogen release from N-heterocyclic liquid organic hydrogen carriers, Commun. Chem. 2 (2019), https://doi.org/10.1038/s42004-019-0167-7.

[45] G.C. Cabilla, A.L. Bonivardi, M.A. Baltanás, Characterization by CO/FTIR spectroscopy of Pd/silica catalysts and its correlation with syn-gas conversion, Catal. Lett. 55 (1998) 147–156, https://doi.org/10.1023/a:1019095231484.

[46] R.F. Hicks, A.T. Bell, Effects of metal-support interactions on the hydrogenation of CO over Pd SiO2 and Pd La2O3, J. Catal. 90 (1984) 205–220, https://doi.org/10.1016/0021-9517(84)90249-5.

[47] A. Setiawan, J. Friggieri, E.M. Kennedy, B.Z. Dlugogorski, M. Stockenhuber, Catalytic combustion of ventilation air methane (VAM)-long term catalyst stability in the presence of water vapour and mine dust, Catal. Sci. Technol. 4 (2014) 1793–1802, https://doi.org/10.1039/c4cy00120f.

[48] L.M. Neal, S.D. Jones, M.L. Everett, G.B. Hoflund, H.E. Hagelin-Weaver, Characterization of alumina-supported palladium oxide catalysts used in the oxidative coupling of 4-methylpyridine, J. Mol. Catal. A Chem. 325 (2010) 25–35, https://doi.org/10.1016/j.molcata.2010.03.024.

[49] J.M. Giraudon, A. Elhachimi, F. Wyrwalski, S. Siffert, A. Aboukaïs, J.F. Lamonier, G. Leclercq, Studies of the activation process over Pd perovskite-type oxides used for catalytic oxidation of toluene, Appl. Catal. B 75 (2007) 157–166, https://doi.org/10.1016/j.apcatb.2007.04.005.

[50] O. Lupan, V. Postica, M. Hoppe, N. Wolff, O. Polonskyi, T. Pauporté, B. Viana, O. Majérus, L. Kienle, F. Faupel, R. Adelung, PdO/PdO2 functionalized ZnO:::Pd films for lower operating temperature H2 gas sensing, Nanoscale 10 (2018) 14107–14127, https://doi.org/10.1039/c8nr03260b.

[51] D.R. Fertal, M. Monai, L. Proaño, M.P. Bukhovko, J. Park, Y. Ding, B. M. Weckhuysen, A.C. Banerjee, Calcination temperature effects on Pd/alumina catalysts: particle size, surface species and activity in methane combustion, Catal. Today 382 (2021) 120–129, https://doi.org/10.1016/j.cattod.2021.08.005.

[52] R. Price, T. Eralp-Erden, E. Crumlin, S. Rani, S. Garcia, R. Smith, L. Deacon, C. Euaruksakul, G. Held, The partial oxidation of methane over Pd/Al2O3 catalyst nanoparticles studied in-situ by near ambient-Pressure X-ray photoelectron spectroscopy, Top. Catal. 59 (2016) 516–525, https://doi.org/10.1007/s11244-015-0520-8.

[53] I. Bondarchuk, F.J.C.S. Aires, G. Mamontov, I. Kurzina, Preparation and investigation of pd and bimetallic pd-sn nanocrystals on γ-al2o3, Crystals (Basel) 11 (2021), https://doi.org/10.3390/cryst11040444.

[54] K. Otto, L.P. Haack, J.E. deVries, Identification of two types of oxidized palladium on γ-alumina by X-ray photoelectron spectroscopy, Appl. Catal. B 1 (1992) 1–12, https://doi.org/10.1016/0926-3373(92)80003-I.

[55] S. Ladas, H. Poppa, M. Boudart, The adsorption and catalytic oxidation of carbon monoxide on evaporated palladium particles, Surf. Sci. 102 (1981) 151–171, https://doi.org/10.1016/0039-6028(81)90313-7.

[56] L. Chen, J. Yan, Z. Tong, S. Yu, J. Tang, B. Ou, L. Yue, L. Tian, Nanofiber-like mesoporous alumina supported palladium nanoparticles as a highly active catalyst for base-free oxidation of benzyl alcohol, Microporous Mesoporous Mater. 266 (2018) 126–131, https://doi.org/10.1016/j.micromeso.2018.02.037.

[57] B. Karimi, H. Behzadnia, M. Bostina, H. Vali, A nano-fibrillated mesoporous carbon as an effective support for palladium nanoparticles in the aerobic oxidation of alcohols "on pure water", Chem. - A Eur. J. 18 (2012) 8634–8640, https://doi.org/10.1002/chem.201200373.

[58] W. Fu, Z. Li, W. Xu, Y. Wang, Y. Sun, Y. Dai, Exceptionally thermal-stable Al2O3/TiO2 nanofibers by depressing surface-initiated grain growth as new supports for anti-sintering Pt nanoparticles, Mater. Today Nano 11 (2020), https://doi.org/10.1016/j.mtnano.2020.100088.

[59] Z. Zhang, K. Sun, Y. Ma, Q. Liu, Q. Li, S. Zhang, Y. Wang, Q. Liu, D. Dong, X. Hu, Nanofibers and amorphous Ni/Al2O3 catalysts - effect of steric hindrance on hydrogenation performance, Catal. Sci. Technol. 9 (2019) 4510–4514, https://doi.org/10.1039/c9cy00985j.

[60] S. Ji, X. Lu, M. Zhang, L. Leng, H. Liu, K. Yin, C. Xu, C. He, J.H. Horton, J. Zhang, Z. Li, Construction of a single-atom palladium catalyst by electronic metal-support interaction and interface confinement effect with remarkable performance in Suzuki coupling reaction, Chem. Eng. J. 452 (2023) 139205, https://doi.org/10.1016/J.CEJ.2022.139205.

[61] J. Liu, Single-atom catalysis for a sustainable and greener future, Curr. Opin. Green. Sustain Chem. 22 (2020) 54–64, https://doi.org/10.1016/J.COGSC.2020.01.004.

[62] X.F. Yang, A. Wang, B. Qiao, J. Li, J. Liu, T. Zhang, Single-atom catalysts: a new frontier in heterogeneous catalysis, Acc. Chem. Res 46 (2013) 1740–1748, https://doi.org/10.1021/AR300361M.

[63] K. Alexopoulos, Y. Wang, D.G. Vlachos, First-principles kinetic and spectroscopic insights into single-atom catalysis, ACS Catal. 9 (2019) 5002–5010, https://doi.org/10.1021/acscatal.9b00179.

[64] M. Vandichel, A. Moscu, H. Grönbeck, Catalysis at the rim: a mechanism for low temperature CO oxidation over Pt3Sn, ACS Catal. 7 (2017) 7431–7441, https://doi.org/10.1021/ACSCATAL.7B02094.